Applied Surface Science 393 (2017) 180–190

Contents lists available at ScienceDirect

Applied Surface Science

journal homepage: www.elsevier.com/locate/apsusc

Full length article

Fabrication of a direct Z-scheme type WO_3/Ag_3PO_4 composite photocatalyst with enhanced visible-light photocatalytic performances

Jinsuo Lu[a,*], Yujing Wang[c], Fei Liu[a], Liang Zhang[b], Shouning Chai[b,*]

[a] School of Environmental and Municipal Engineering, Xi'an University of Architecture and Technology, Xi'an 710055, China
[b] College of Sciences, Xi'an University of Architecture and Technology, Xi'an 710055, China
[c] School of Materials and Chemical Engineering, Xi'an Technological University, Xi'an, Shaanxi 710032, China

ARTICLE INFO

Article history:
Received 18 July 2016
Received in revised form 1 October 2016
Accepted 3 October 2016
Available online 3 October 2016

Keywords:
Z-scheme photocatalyst
Silver orthophosphate
Nanocomposites
Organic dye degradation

ABSTRACT

A direct Z-scheme type photocatalyst WO_3/Ag_3PO_4 composite (molar ration 1:1, 1W/1Ag) was prepared by hydrothermal method. The 1W/1Ag was characterized by scanning electron microscopy (SEM), X-ray powder diffraction (XRD), UV–vis diffuse reflection spectroscopy (DRS), X-ray photoelectron spectroscopy (XPS), and photoluminescence emission spectroscopy (PL) etc. technologies. The photocatalytic performances were evaluated by degradation of methylene blue (MB) and methyl orange (MO), and their removal rates were up to 95% after 60 min and 90% after 180 min, respectively. The prepared 1W/1Ag exhibits a much higher photocatalytic activity than pure Ag_3PO_4 and pure WO_3 under visible light irradiation. The apparent rate constants of MB and MO degradation on 1W/1Ag are about 2.4 and 2.5 times that of pure Ag_3PO_4, respectively. The enhanced performance of the 1W/1Ag is attributed to a synergistic effect including relatively high surface area, strong light absorption, matched energy band structure, and the improved separation of photogenerated charge carriers between the two components. A reasonable Z-scheme mechanism referring to directed migration of photoinduced carriers was proposed. Thus, it can be suggested that the 1W/1Ag can serve as a promising photocatalyst for environmental purification and clean energy utilization.

1. Introduction

As a promising technology, photocatalysis has been widely studied in various fields such as environmental purification, solar energy conversion, and water splitting, etc [1–3]. However, there are still several problems in photocatalysis, such as poor utilization of solar light, low photo-to-current efficiency, and weak stability [4,5]. To utilize sunlight efficiently, a great deal of visible light responsive photocatalysts were developed over the past decades, including binary semiconductors WO_3, CdS, MoS_2, g-C_3N_4, ternary compounds $CuFe_2O_4$, $ZnIn_2S_4$, BiOX(X = Cl, Br, I), etc [6–13]. In recent, as a new-type photocatalyst, Ag-based photocatalysts have attracted considerable attention for organic pollutants removal. Particularly, Ag_3PO_4 is considered as a promising visible light responsive photocatalyst due to its narrow indirect and direct band gap of 2.36 eV and 2.43 eV, respectively [14–17]. Yi et al. reported that Ag_3PO_4 exhibits extremely high capability in the O_2 evolution from photooxidation of water and decomposition of organic dye under visible light, and the quantum efficiencies achieved up to 90% at wavelengths greater than 420 nm, which prominent photocatalytic performances may be ascribed to the inductive effect of PO_4^{3-} and the dispersive conduction band [18]. Zhu et al. revealed that the relatively low valence band level is favorable of its oxidizing ability, meanwhile, the π^* orbit in the conduction band improves the electrons migration rate and separation efficiency of photo-generated charge carriers [19]. To further improving Ag_3PO_4 photoelectric and photocatalytic activity, some efforts have been devoted to modulate its shape, morphology, and crystal facet [20–23], and others are interested in developing novel Ag_3PO_4-based bi/multi- component photocatalysts [16,24,25].

In recent years, Z-scheme photocatalysis process inspired by natural photosynthesis in green plants is considered as an efficient system for water splitting, in which two different photocatalysts with proper band energies are combined via a suitable shuttle redox mediator [26–28]. Comparing with conventional single component water splitting systems, each photocatalyst in the Z-scheme

* Corresponding authors.
E-mail addresses: lujinsuo@xauat.edu.cn (J. Lu), s.n.chai@xauat.edu.cn (S. Chai).

http://dx.doi.org/10.1016/j.apsusc.2016.10.003
0169-4332/

system is only responsible for one half-reaction (H_2 evolution reaction or O_2 evolution reaction), and visible light could be utilized more efficiently in Z-scheme system because the energy required to drive each photocatalyst is reduced. Similar to the heterojunction-type photocatalyst composites, the Z-scheme system also features the spatial isolation of photogenerated carriers, which reduces the probability of bulk electron-hole recombination. Moreover, the shuttle redox mediator participates and optimizes the process of electron transfer in the complex redox reactions. Generally, some soluble redox ion pairs, including Fe^{3+}/Fe^{2+}, IO_3^-/I^-, $[Co(bpy)_3]^{3+/2+}$/$[Co(phen)_3]^{3+/2+}$ etc. were selected as suitable redox mediators and greatly enhance the activity for overall water splitting in the liquid-state Z-scheme systems [29–31]. In 2006, Tada et al. firstly prepared all-solid-state Z-scheme photocatalyst of CdS/Au/TiO_2, where anchored solid Au nanoparticles between CdS and TiO_2 acted as electron transfer mediator [32]. This three-component system exhibits excellent activity, far exceeding those of the single/two component systems, because the photogenerated electrons in the conduction band of TiO_2 could be transferred through the Au medium and recombine with the photogenerated holes left in valance band of CdS. Thus, the photogenerated electrons and holes are accumulated in the conduction band of CdS and the valance band of TiO_2, respectively. Besides the noble metals, some nonmetals also were used for transferring Z-scheme electron. Amal et al. found that the reduced graphene oxide could serve as electron transfer when it was embedded between $BiVO_4$ and Ru/$SrTiO_3$:Rh [33]. It is clear that either liquid-state or solid-state redox mediators play important roles in shuttling the photogenerated carriers in Z-scheme systems [34–36]. However, the presence of a shuttle redox mediator would also cause some drawbacks, such as light-shielding effect, competitive oxidation of redox couples, and high cost of noble metal etc. So it is an advisable choice to construct mediator-free direct Z-scheme systems only consisting of two components, which would drew more and more attention. More recently, it was demonstrated that many Ag_3PO_4 based photocatalytic systems, such as g-C_3N_4-Ag_3PO_4, graphene-Ag_3PO_4 hybrid photocatalysts show a direct Z-scheme mechanism without an electron mediator [37,38]. These composite can not only effectively avoid the Ag_3PO_4 dissolution, but also improve their photocatalytic activity due to the quick separation of photogenerated charge carriers. Thus, it is a promising alternative to fabricate a novel direct Z-scheme Ag_3PO_4 based photocatalyst for promoting its overall catalytic performance.

In this work, tungsten oxide (WO_3), an environment-friendly semiconductor material with narrow band gap (2.4–2.8 eV) and good stability in aqueous media was employed to combine with the Ag_3PO_4 to obtain WO_3/Ag_3PO_4 hybrid photocatalyst [39,40]. Firstly, a facile double-step hydrothermal method was applied to prepare WO_3/Ag_3PO_4, following by SEM, XRD, UV–vis DRS, IR, PL, and XPS characterizations. Secondly, the photocatalytic activities of the WO_3/Ag_3PO_4 composite were evaluated by the degradation of methylene blue (MB) and methyl orange (MO) under visible light. Finally, the relevant photocatalytic mechanism was investigated and the stability of the WO_3/Ag_3PO_4 composite was also examined.

2. Experimental section

2.1. Reagents and materials

All reagents used in this study were analytical grade. Sodium tungstate dehydrate, sodium chloride, silver nitrate, disodium hydrogen orthophosphate, and hydrochloric acid were purchased from Sigma-Aldrich Chemical Co., Ltd. MB and MO were purchased from Sinopharm (Shanghai, China). Double distilled Millipore water was used for all the experiments.

2.2. Synthesis of catalysts

2.2.1. Synthesis of Ag_3PO_4

20 mL of 0.1 mol L^{-1} Na_2HPO_4 solution was added dropwise in a beaker containing 60 mL of 0.1 mol L^{-1} $AgNO_3$ solution at 25 °C within 10 min. The mixture was magnetically stirred till yellow precipitate formed. Then, the suspension was transferred into a 100 mL Teflon-lined stainless steel autoclave, and kept at 120 °C for 6 h. Finally, the sample was washed with deionized water three times and then was dried under vacuum at 80 °C for 6 h.

2.2.2. Synthesis of WO_3/Ag_3PO_4 composite

The first step is to prepare WO_3 by a simple hydrothermal process. In brief, 10 mL of 2.0 mol L^{-1} HCl solution was dropped in 30 mL of 0.1 mol L^{-1} $Na_2WO_4{\cdot}2H_2O$ with magnetically stirred at 25 °C. Then, the obtained suspension was transferred into a 50 mL Teflon-lined stainless steel autoclave and kept at 180 °C for 48 h. After that, the precipitate was treated by filtration, washed several times with distilled water, and dried at 80 °C for 6 h. The sample was sintered at 450 °C for 2 h and WO_3 was obtained.

The second step is to fabricate WO_3/Ag_3PO_4 composite. Typically, an appropriate amount of previous prepared WO_3 powder (0.46 g) was dispersed in 60 mL of 0.1 mol L^{-1} $AgNO_3$ solution by sonication for 10 min and subsequently agitation for 20 min, followed by dropwise addition of 20 mL of 0.1 mol L^{-1} Na_2HPO_4 solution under stirring at 25 °C. The suspension was also transferred into a 100 mL Teflon-lined stainless steel autoclave and kept at 120 °C for 6 h. And then the sample was washed with deionized water and vacuum-dried at 80 °C for 6 h. Finally, the WO_3/Ag_3PO_4 composite with 1:1 molar ratio of WO_3 against Ag_3PO_4 was obtained, which was labeled as 1W/1Ag. For comparison, other two WO_3/Ag_3PO_4 samples with two different molar ratio of WO_3 against Ag_3PO_4 (2:1 and 1:2) were prepared in a similar procedure, which were labeled as 2W/1Ag and 1W/2Ag.

2.3. Characterization of the as-prepared photocatalysts

The morphology of samples was characterized by a scanning electron microscopy (EFEG-SEM, Model Quanta 200 FEG, FEI). X-ray diffraction (XRD, Model D/max2550VB3+/PC, Rigaku) analysis was performed using a diffractometer with Cu Kα radiation, operated at accelerating voltage of 40 kV and current of 30 mA. UV–vis diffusive reflectance spectra (DRS) were determined using a JASCO V-550 UV–vis spectrometer. Fourier transform infrared spectra (FT-IR) was recorded on a Bruker VERTEM 70 spectrophotometer, using KBr powder containing *ca.* 1 wt% of the sample. The XPS spectra of 1W/1Ag composite were determined on a X-ray photoelectron spectrometer (AXIS-ULTRA DLD, Shimadzu, Japan) using monochromatized Al Kα radiation (1486.6 eV). The binding energy (BE) measurements were corrected for charging effects with reference to the C1 s peak of the adventitious carbon (284.6 eV). The specific surface area of the samples was estimated by the BET adsorption-desorption isotherms of nitrogen at 77 K using a BET analyzer (TRISTAR 3000 Micromeritics, U.S.), and the samples were out gassed at 180 °C in vacuum for 6 h. The photoluminescence emission spectra (PL) were collected on an F-7000 Fluorescence spectrophotometer (Hitachi, Japan) at room temperature, using a Xe lamp as light source. Photocurrent measurement was carried out in a three-electrode cell system of CHI 660E (CHI Co., USA) electrochemical workstation. A saturated calomel electrode (SCE) served as the reference and Pt foil as the counter electrode. The working electrodes were prepared refers to the literature reported [8]. Firstly, a F-doped SnO_2 (FTO) glass pieces with a size of 1.5 × 6 cm was sonicated in acetone for 10 min, and then rinsed with deionized water and dried. Secondly, 0.1 g of photocatalyst mixed with 0.05 g of polyethylene glycol (PEG 2000) in a small mortar, and

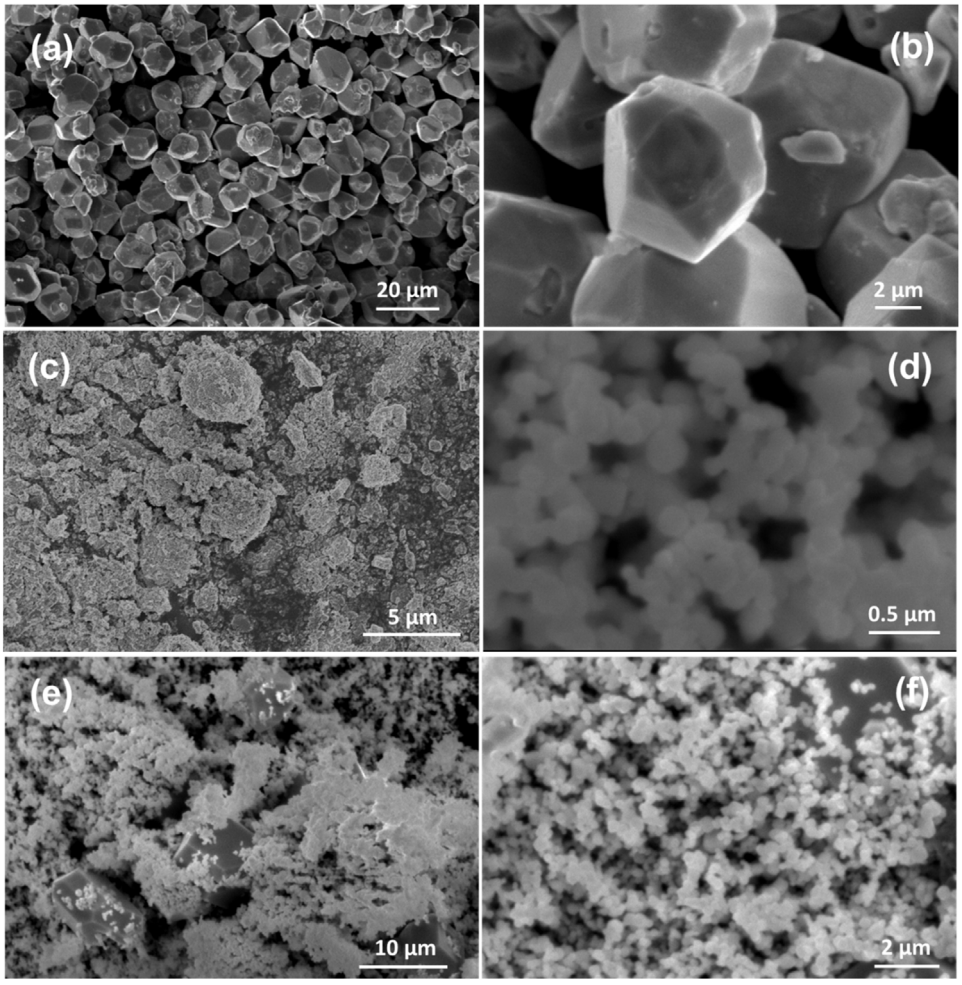

Fig. 1. SEM images of Ag_3PO_4 (a,b), WO_3 (c,d), and 1W/1Ag (e,f), (a,c,e) corresponding to low magnification, (b,d,f) corresponding to high magnification.

ground to form slurry with adding 1.0 mL ethanol. The slurry was coated onto FTO using a doctor blade method. The electrode was dried at 80 °C in a drying oven and calcined at 300 °C for 60 min in air atmosphere. The electrochemical impedance spectroscopy (EIS) were recorded by applying an AC voltage of 10 mV amplitude in the frequency range of 10^5 Hz –10^{-2} Hz with the initial potential (0 V). The working area of working electrode is 4 cm^2, and the electrolyte is 0.1 mol L^{-1} Na_2SO_4 solution.

2.4. Evaluation of photocatalytic activity

The performance of the photocatalyts was evaluated through the photocatalytic degradation of MB/MO under visible light. The photocatalytic degradation was carried out in a photochemical reactor equipped with a magnetic stirrer and a jacketed cooler to maintain a constant temperature (25 ± 2 °C). A 300 W Xenon lamp (CeauLight, CEL-HXF300) equipped with an ultraviolet cutoff filter provided visible light with λ >420 nm. In a typical photocatalytic measurement, 0.1 g of the as-prepared photocatalysts was dispersed into 100 mL of MB or MO solution with an initial concentration of 10 g mL^{-1} via ultrasonication for 2 min. To reach an adsorption–desorption equilibrium, the suspension was stirred in the dark for 30 min before light irradiation. Then, 2 mL of suspensions was taken out at given time intervals and separated by centrifugation. The concentrations of MB and MO during degradation were measured by a UV–vis spectrophotometer (UV-2550, Shimadzu, Japan) at the wavelength of 664 nm and 463 nm, respectively. The photocatalytic degradation efficiency of MB/MO over the photocatalyst was calculated from the following equation:

$$\text{Degradation efficiency} = (1 - C/C_0) \times 100\% \quad (1)$$

where C_0 and C are the concentration in the initial time and after illumination time t of MB/MO.

To test the stability of the 1W/1Ag photocatalyst, it was recycled and reused three times in the decomposition of MB/MO under the same conditions. After each degradation experiment, the residual suspensions was centrifuged to recycle the photocatalyst powders, all of used photocatalysts were collected then dried at 100 °C for next test.

3. Results and discussion

3.1. Characterization

The microscopic morphologies of pure Ag_3PO_4, WO_3 and 1W/1Ag were determined by SEM. Fig. 1(a,b), a typical SEM image of Ag_3PO_4 at different magnification, shows the sample is composed of large quantities of polyhedral particles with size of 10 to 15 μm. The large size would be due to the relatively high hydrothermal temperature in the hydrothermal process. The edges and angles of the crystalline grains are regular and distinct, while some defects can be found on crystal surfaces. It had been demonstrated that all of these would act as active sites for degradation reaction. From Fig. 1(c,d), it is also found that the diameter of WO_3 nanoparticle

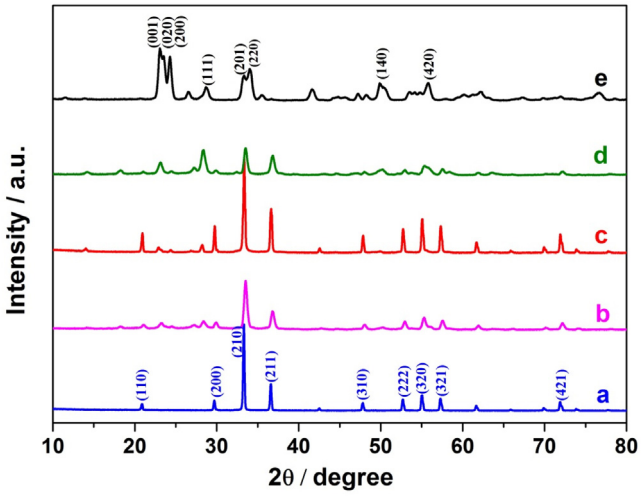

Fig. 2. XRD patterns of Ag_3PO_4 (a), 1W/2Ag (b), 1W/1Ag (c), 2W/1Ag (d), and WO_3 (e).

is about 200–300 nm, and the particle size is relatively uniform, which endows its higher specific surface area and larger surface energy than micro-sized Ag_3PO_4 grain. For the 1W/1Ag (Fig. 1(e,f)), the spherical-like WO_3 particles covers almost all the crystal surface of Ag_3PO_4, however, the morphology and particle size is not obviously change after composition. Although a portion of WO_3 agglomerates, the combination between WO_3 and Ag_3PO_4 interfaces are firm and compact. Obviously, such contact is favorable to mediate charge transfer during photocatalytic oxidation.

To identify the phase composition and crystal structure of the samples, XRD analysis was conducted. Fig. 2 shows the XRD patterns of Ag_3PO_4, WO_3, and WO_3/Ag_3PO_4 composites with different molar ration of WO_3 to Ag_3PO_4 (i.e. 1W/1Ag, 1W/1Ag and 2W/1Ag). For pure Ag_3PO_4, the characteristic diffraction peaks at 2θ value 21.7°, 29.7°, 33.3°, 36.5°, 47.8°, 52.6°, 54.9°, 57.2°, and 71.8° corresponding to (110), (200), (210), (211), (310), (222), (320), (321), and (421) facets, which could be indexed to the body-centered cubic structure (JCPDS No.06-0505) [39,40]. While for pure spherical WO_3, the peaks at 23.1°, 23.7°, 24.1°, 28.8°, 33.6°, 34°, 50° and 55.4° are respectively corresponded to the (001), (020), (200), (111), (201), (220), (140), (420) crystal planes, confirming the existence of the orthorhombic structure of WO_3 (JCPDS No. 20-1324). These results are in good accordance with previous studies [6,37,41]. As shown in Fig. 2(b,c,d), both of the characteristic diffraction peaks of Ag_3PO_4 and WO_3 can be observed in the XRD patterns of WO_3/Ag_3PO_4 composites, indicating that WO_3 nanoparticles successfully combined with polyhedral Ag_3PO_4. Meanwhile, no XRD additional diffraction peaks can be observed except for those of Ag_3PO_4 and WO_3. In terms of WO_3/Ag_3PO_4 composites, the peak corresponding to the (111) crystal plane of WO_3 gradually becomes stronger with increasing of WO_3 loading content on Ag_3PO_4. Compared to WO_3, the intensity of the diffraction peaks of Ag_3PO_4 is relatively strong, which should be attributed to its larger micron-sized crystalline grain. Moreover, the addition of WO_3 did not obviously change the diffraction peak positions of Ag_3PO_4, implying that WO_3 was not incorporated into the Ag_3PO_4 lattice.

As is known to all, the optical absorption property is an important prerequisite for photocatalysis, hence UV–vis DRS are employed to detect the optical absorption of five catalysts. Fig. 3(a) shows the DRS of Ag_3PO_4, WO_3, 1W/1Ag, 1W/1Ag, and 2W/1Ag. The bare Ag_3PO_4 shows a strong absorption peak at ~265 nm and have an absorption edge at ~520 nm whereas pure WO_3 shows absorption at around 460 nm [42]. The optical spectra show that the total absorption strength of WO_3/Ag_3PO_4 composite is enhanced when

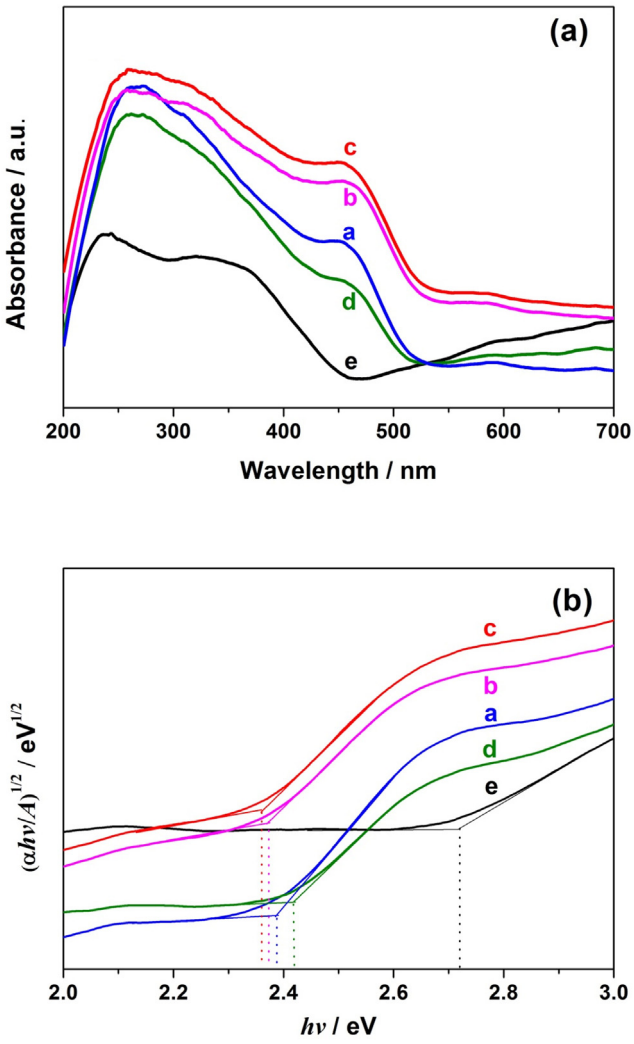

Fig. 3. UV–vis DRS and band gap energies of Ag_3PO_4 (a), 1W/2Ag (b), 1W/1Ag (c), 2W/1Ag (d), and WO_3 (e).

an appropriate amount of WO_3 coupled with Ag_3PO_4 (1W/2Ag and 1W/1Ag) and a slight red shift of absorption edge. It indicates that WO_3/Ag_3PO_4 composite absorbs visible light more effective than either of bare samples. In addition, with an appropriate loading content of WO_3, the WO_3/Ag_3PO_4 composites (1W/2Ag and 1W/1Ag) show enhanced absorption intensity nearly in whole light region. The probable reason is innumerable pores and lacunas with different size were formed in the WO_3/Ag_3PO_4 composites due to the mismatching of particle size during WO_3 nanoparticle combined with Ag_3PO_4 micro-grain. These cavities could obviously increase the photon-matter interaction length via refraction and reflection and produce slow photon effect, resulting in the enhanced absorption ability in the range of 200–700 nm. Obviously, the absorption intensity of 2W/1Ag is decrease with the WO_3 content excesses optimal amounts, attributing to those effects weaken when excessive compact packing of WO_3.

The band gap energy (E_g) of the semiconductors could be determined using the following equation:

$$\alpha h\nu = A(h\nu\text{-}E_g)^n \quad (2)$$

where α is absorption coefficient, h is Planck's constant, ν is the frequency of light, A represents a constant number, and n equals 2 for Ag_3PO_4 and WO_3 (indirect transition) [43–46]. Fig. 3(b) plots the absorption spectra as $(\alpha h\nu)^{1/2}$ *vs.*$h\nu$. We deduced the values of

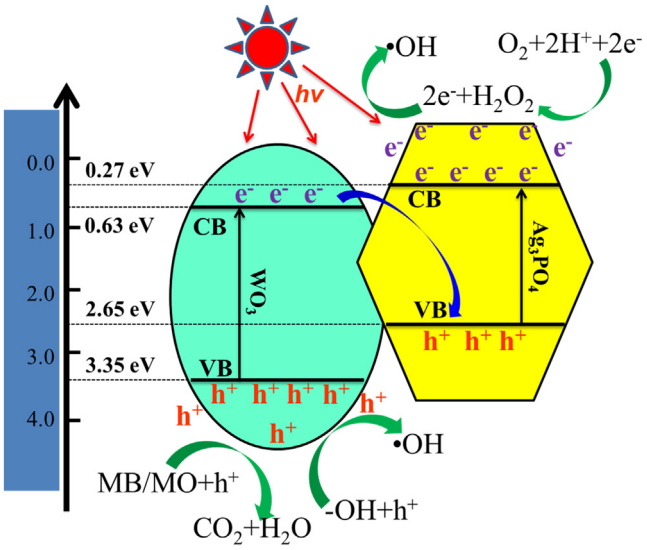

Fig. 4. Proposed mechanism for the direct Z-scheme charge-carrier transfer process in the 1W/1Ag composite.

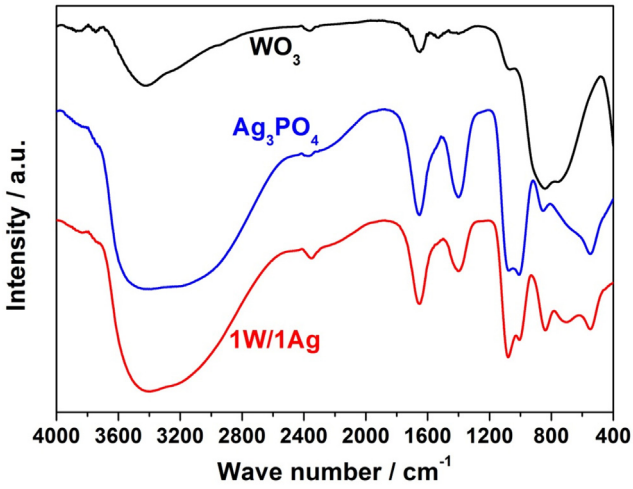

Fig. 5. FT-IR spectra of Ag_3PO_4, 1W/1Ag, and WO_3.

E_g for WO_3, Ag_3PO_4, 1W/2Ag, 1W/1Ag and 2W/1Ag are 2.72 eV, 2.38 eV, 2.37 eV, 2.36 eV, and 2.42 eV, respectively, which corresponds well with the previously reported results [24,47]. The result indicates that the combination of WO_3 reduce the E_g for Ag_3PO_4. In short, 1W/1Ag shows the most outstanding photochemical properties among three WO_3/Ag_3PO_4 composites, so it is selected as the representative photocatalyst in following study.

The electronic band structure of typical 1W/1Ag can be estimated according to the following empirical equations [43,48]:

$$E_{VB} = \chi - E^e + 0.5E_g \quad (3)$$

$$E_{CB} = E_{VB} - E_g \quad (4)$$

where E_{VB} and E_{CB} are the valence and conduction band potentials, respectively; χ is the electronegativity of the semiconductor, the values for Ag_3PO_4 and WO_3 are 5.96 and 6.49 eV, respectively; E^e is the energy of free electrons on the hydrogen scale (about 4.5 eV vs. NHE). It can be calculated that the E_{VB} of Ag_3PO_4 and WO_3 are about 2.65 and 3.35 eV vs. NHE, and the corresponding E_{CB} are 0.27 and 0.63 eV vs. NHE, respectively, as depicted in Fig. 4.

A comparison of 1W/1Ag to pure Ag_3PO_4 and WO_3 in functional groups of the chemical structure was conducted by FT-IR spectroscopy, as depicted in Fig. 5. In the spectra of all the three samples, the strong and broad absorption around 3300 cm^{-1} is ascribed to the stretching vibration of O—H. Both sharp bands at 1400 and 1655 cm^{-1} are attributed the bending vibration of H—O—H of adsorbed water molecules [49]. In the crystalline structure of WO_3, tungsten atoms are located in the center of WO_6 octahedra with oxygen at the vertices forming W-O-W connections. The IR active bands include fundamental vibrations of W=O, W—O and W—O—W [50]. For the pure WO_3, the characteristic peaks at *ac.* 840 and 1404 cm^{-1} associated with stretching vibrations of W—O—W and W—OH respectively [51]. For the pure Ag_3PO_4 and 1W/1Ag, the peak at *ca.* 550 cm^{-1} is related to the O=P–O bending vibration, while the peaks at *ca.* 850 and 1010 cm^{-1} are respectively assigned to the symmetric and asymmetric stretching vibration modes of P—O—P [52]. All the characteristic peaks of Ag_3PO_4 and WO_3 can be observed in the spectra of 1W/1Ag.

XPS with high sensitivity is used to study the surface chemical state of the 1W/1Ag. As shown in Fig. 6(a), the XPS survey spectrum suggested that Ag, W, O, and P elements existed in this material, being coincident with the constituent of the composites. In addition, detailed speciation information is investigated from high resolution XPS scans in the different binding energy regions. The Ag 3d spectrum (Fig. 6b) display a doublet characteristic centered at 374.1 and 368 eV, which could be assigned to $Ag3d_{3/2}$ and $Ag3d_{5/2}$ of typical Ag^+, respectively [40,53,54]. For the W 4f XPS spectra depicted in Fig. 6(c), the observed W 4f consisted of a single doublet at binding energies of 35.8 eV for W $4f_{7/2}$ and 37.9 eV for W $4f_{5/2}$. It can be reasoned that tungsten is present in the W^{6+} oxidation state of the WO_3 [49,55]. The O 1 s spectrum in Fig. 6(d) can be deconvoluted into two peaks, the binding energy of ca. *ca.* 530.6 eV was ascribed to the lattice oxygen in the Ag_3PO_4 and WO_3, while the peak at *ca.* 531.9 eV probably corresponded to the hydroxyl group [52]. The XPS results of the surface composite photocatalyst characters are coincident well with the XRD and IR results aforementioned.

3.2. Photocatalytic performances

MB and MO were selected as probe molecules of organic pollutants to evaluate the photocatalytic activity of 1W/1Ag, which are two kind of common contaminants in industrial wastewater. Prior to each photocatalysis test, the mixture of catalysts and pollutants was stirred in the dark for 30 min, the timing for photocatalysis test started. Fig. 7 shows the photocatalytic performance of the pure WO_3, Ag_3PO_4 and 1W/1Ag under visible light illumination. Two blank tests without using any photocatalyst confirmed that the self-photolysis of MB and MO are negligible. The 1W/1Ag exhibits notably higher photocatalytic activity than pure WO_3 and Ag_3PO_4 for both pollutants. After 60 min irradiation, above 95% of MB decomposed in the presence of 1W/1Ag photocatalyst, while only 70% and 55% are removed within the same time using pure Ag_3PO_4 and WO_3, respectively. During MO photocatalytic degradation, MO exhibits higher stability than MB in the water environment. About 90% of MO is removed with 1W/1Ag after 180 min. However, 61% and 27% of MO are eliminated from the solution with pure Ag_3PO_4 and WO_3, respectively. The lowest catalytic activity of WO_3 is mainly attributed to the more positive conduction band potential of WO_3, which does not favor the production of oxidizing species derived from electrons, such as H_2O_2 and •OH etc. In addition, wide band gap of WO_3 results in less absorption of visible light ($\lambda > 460$ nm). While for 1W/1Ag catalyst, the outstanding photocatalytic activity can be ascribed to highly effective separation of photogenerated electron–hole pairs and synergic effect between them.

To further understand the enhanced performance of 1W/1Ag, the kinetics for MB and MO decay is analyzed in detail. The photo-

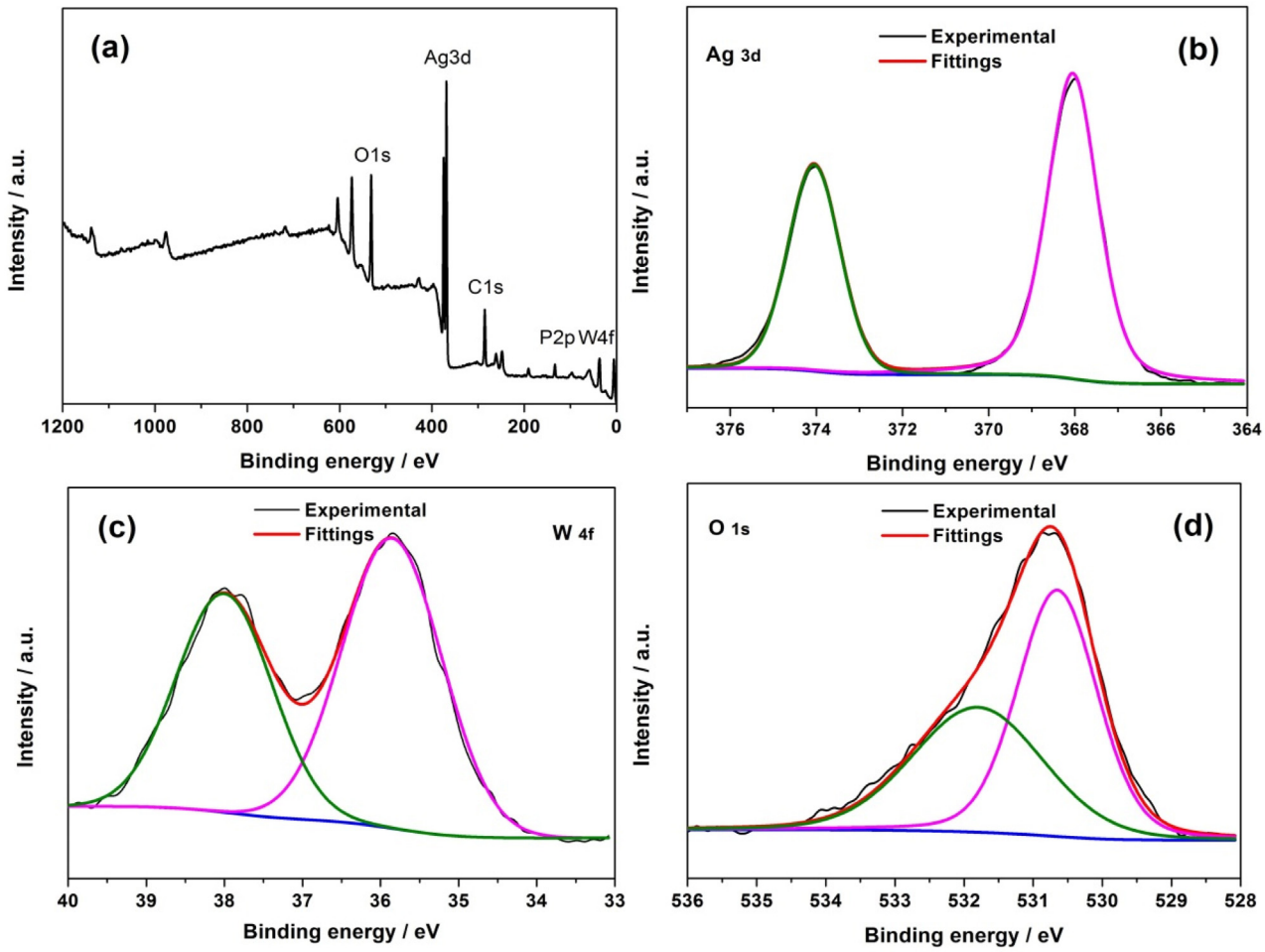

Fig. 6. XPS spectra of the 1W/1Ag, survey spectrum(a), Ag 3d (b), W 4f (c)and O 1s (d).

catalytic degradation of MB and MO follow the pseudo-first-order kinetic model $\ln(C/C_0) = -kt$, where C_0, and C is the initial concentration and instant concentration at time t, respectively, t is the reaction time, and k is the rate constant [39]. The linear relationship is shown in Fig. 8. For MB decomposing, the apparent rate constant of 1W/1Ag is 0.048 min^{-1}, which is 2.4, and 4.0 times that of pure Ag_3PO_4, and WO_3, respectively. The same tendency could be observed in MO degradation, the apparent rate constant of 1W/1Ag (0.012 min^{-1}) is the highest among three samples. These results demonstrated that the synergistic effect between Ag_3PO_4 and WO_3 played an important role in enhancing the photocatalytic activity under visible light irradiation. In conclusion, the enhanced performance of 1W/1Ag is mainly attributed to high surface area, strong light absorption and improved separation of photogenerated charge carriers.

The textural properties of the Ag_3PO_4 and 1W/1Ag were investigated by nitrogen sorption analysis. The nitrogen adsorption–desorption isotherms and the pore size distribution (inset) are exhibited in Fig. 9. It can be seen that the pure Ag_3PO_4 and 1W/1Ag have isotherms of type IV and type H3 hysteresis loop, with the hysteresis shaping more like that for the slit-like pores and covering a broad relative pressure range of 0.7–0.95, indicating their large porosity. The pore distributions of the two samples are very broad, illustrating the existence of mesopores and macropores. The BET surface area of the Ag_3PO_4 and 1W/1Ag are 8 $m^2 g^{-1}$ and 35 $m^2 g^{-1}$, respectively. The enhancement of BET surface area of 1W/1Ag is ascribed to the loading WO_3 nanoparticle. The higher surface area not only can provide more photocatalytic active site, but also accelerates mass transfer of the organic dyes during photocatalysis.

The effect of the 1W/1Ag direct Z-scheme construction on the charge separation was investigated via electrochemical impedance spectroscopy (EIS) and photocurrent (i-t) experiments [56]. Fig. 10 (a) shows the EIS response of Ag_3PO_4, 1W/1Ag, and WO_3. Generally, the size of arc radius on the Nyquist plot is related to the resistance of electron transfer and the separation efficiency of photogenerated electrons and holes on the electrode surface. It also shows the energy barrier of electrode reaction. The electron transfer resistance (R_{et}) obtained on the 1W/1Ag is about 80 Ω, which indicates that it has the highest efficiency in charge separation and electron transfer. Forthermore, the photoexcited charge carriers are detected by transient photocurrent responses under visible-light illumination with an on-and-off cycle mode. The higher photocurrent intensity often illustrates the stronger light absorption (in Fig. 3) and higher separation efficiency of holes and electrons. It is obviously found that 1W/1Ag shows much higher photocurrent density than that of pure Ag_3PO_4 and WO_3, and the photocurrent on the 1W/1Ag electrode reaches 2.0 μA, which is 1.7 times and 2.2 times that of Ag_3PO_4 and WO_3, respectively. It means that Z-scheme type is preferable for charge separation and transfer, thus rendering the improvement of the photocatalytic degradation chance to organic dyes.

In general, photoluminescence (PL) emission spectra are also an effective means to explore the mitigation, transfer and recombination process of photo-generated carries for photocatalyst [47,57]. PL spectra were examined for Ag_3PO_4, 1W/1Ag, and WO_3 with

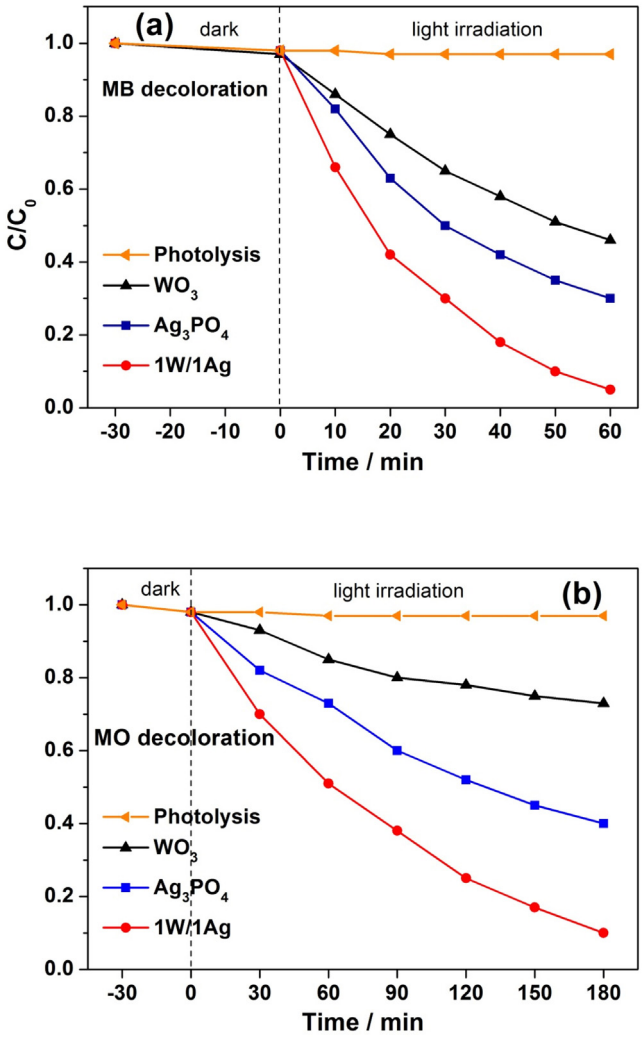

Fig. 7. Concentration change of MB (a), and MO (b) as the function of the illumination time.

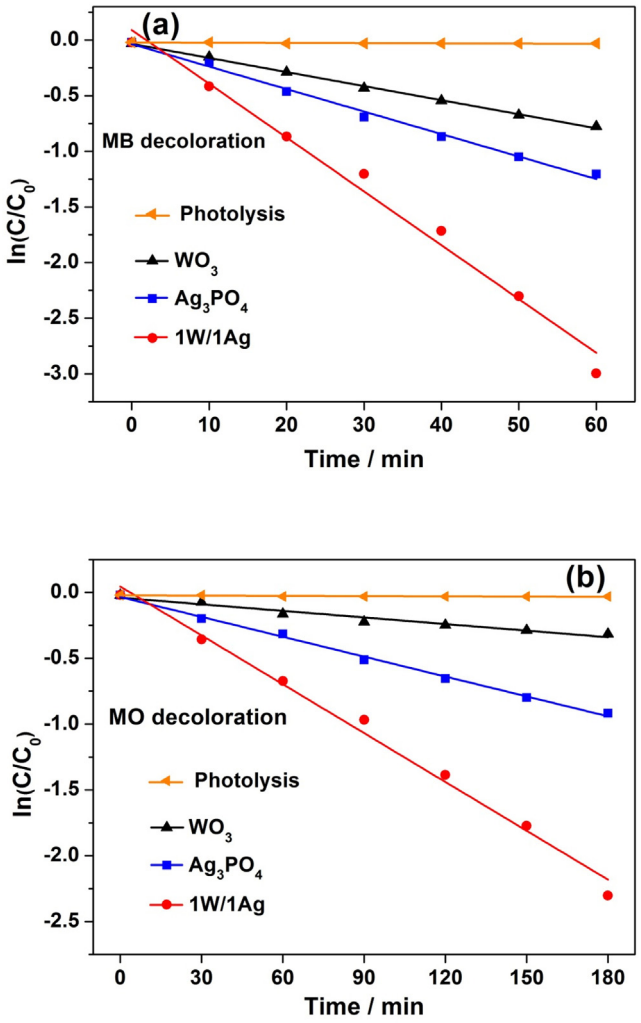

Fig. 8. The first-order kinetics of MB (a) and MO (b) photocatalytic degradation.

an excitation wavelength of 210 nm. As shown in Fig. 11, pure Ag_3PO_4 display two apparent characteristic emission peak centered at about 510 nm and 545, respectively, which was ascribed to the band gap recombination of electron-hole pairs. Comparing with that of pure Ag_3PO_4, the PL intensity of 1W/1Ag was sharply weakened, which indicates the recombination of electron-hole pairs is effectively inhibited. The results are highly in coincident with the results of the EIS and i-t experiments. In order to further understand the photocatalytic mechanism and explore the active species involved in the photocatalytic process, hydroxyl radicals (•OH) were detected on the surface of 1W/1Ag by the PL method using terephthalic acid (TA) as a probe molecule [56,58,59]. According to the reported literatures, the brief experimental procedures were as follows: 0.1 g of the 1W/1Ag powder was dispersed in a mixed aqueous solution of 5×10^{-4} M TA and 2×10^{-3}M NaOH at 25 °C. The visible light was irradiated and solution samples dealing with filter was analyzed every 10 min on a Hitachi F-7000 fluorescence spectrophotometer. The excited wavelength was selected 315 nm. For the 1W/1Ag, it is observed that PL intensity at about 425 nm gradually enhance with increasing irradiation time as shown in Fig. 11, which indicates the production of •OH radical. The results demonstrate that the •OH radical is the main active oxygen species in the photocatalytic degradation.

Essentially, the photocatalytic oxidation and reduction abilities of a semiconductor are related with the potentials of the valence and conduction bands, respectively. The photoexcited electrons generated from Ag_3PO_4 and WO_3 cannot reduce O_2 to $^{\bullet}O_2^-$ or $^{\bullet}HO_2$, because the standard redox potentials of $E^{\theta}(O_2/^{\bullet}O_2^-)$ (−0.33 eV vs. NHE) and $E^{\theta}(O_2/^{\bullet}HO_2)$ (−0.05 eV vs. NHE) are more negative than their conduction band edge potential ($E_{CB}(Ag_3PO_4) = 0.27$ eV, $E_{CB}(WO_3) = 0.63$ eV vs. NHE) [60–62]. Nevertheless, the photoexcited holes generated from Ag_3PO_4 and WO_3 can oxidize OH^- to •OH by reason of their valence band potentials are more positive than the standard redox potential of $OH^-/^{\bullet}OH$ (E^{θ} ($OH^-/^{\bullet}OH$) = 2.4 eV) [43]. On the basis of above experimental facts and analysis, it can be speculated that a possible direct Z-scheme system photocatalyst may be formed when WO_3 is combined with Ag_3PO_4, stemming from the relative short distance between the valence band of Ag_3PO_4 and the conduction band of WO_3, as depicted in Fig. 4 [63]. Under visible light illumination, both Ag_3PO_4 and WO_3 could be excited to produce amounts of electrons and holes simultaneously, whereas those photo-generated charge carriers of Ag_3PO_4 are likely to recombine quickly without introduction of WO_3, leading to the relatively low photocatalytic activity. According to the schematic diagram, the mechanism of the Z-scheme 1W/1Ag for photocatalytic degradation is proposed [59,64,65]. After forming a heterojunction, the electrons in the conduction band of WO_3 timely transfer to the valence band of Ag_3PO_4 and combine with holes there. The holes retaining in the

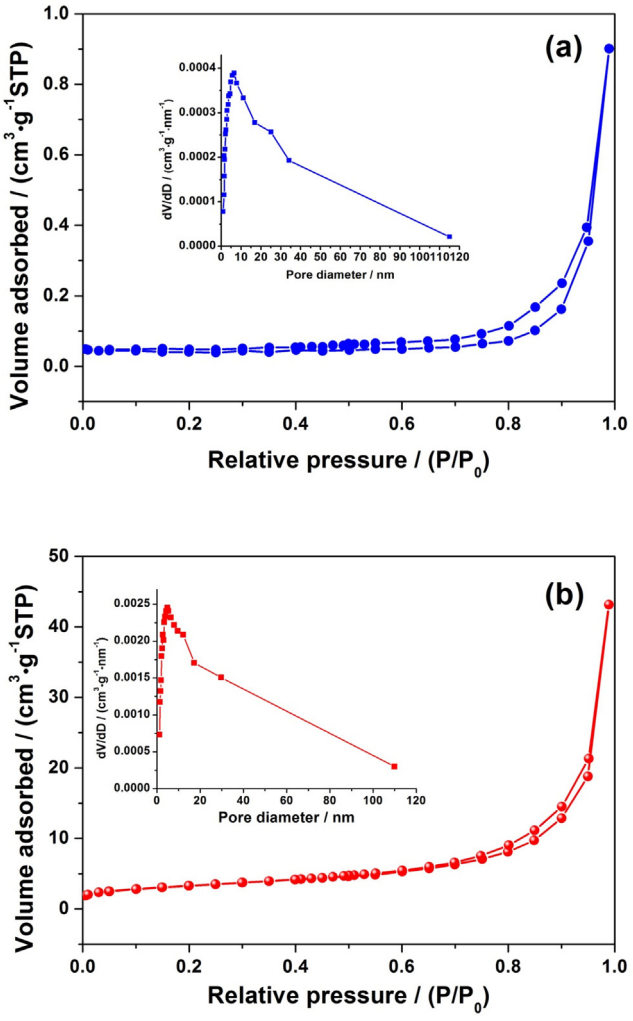

Fig. 9. Nitrogen adsorption-desorption isotherms and corresponding pore-size distribution curves (inset) of Ag_3PO_4 (a), and 1W/1Ag (b).

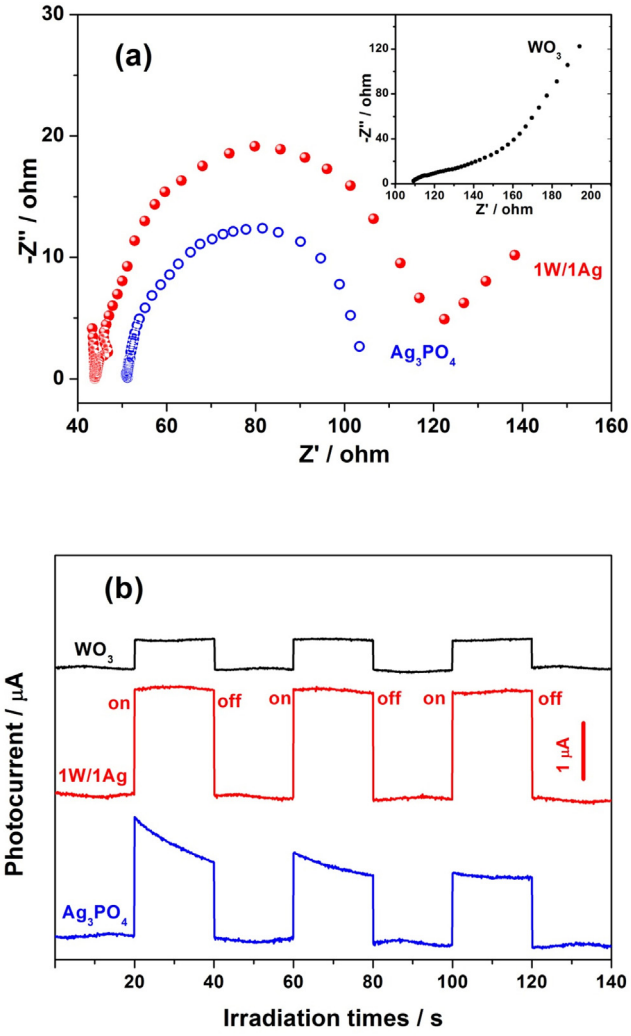

Fig. 10. Electrochemical impedance spectroscopy (a), and transient photocurrent responses (b) of Ag_3PO_4, 1W/1Ag, and WO_3.

valence band of WO_3 could directly oxidize the adsorbed organic dyes to intermediates and even CO_2 and H_2O or indirectly oxidize OH^- to $^\bullet OH$, triggering a series of degradation reactions. The electrons existing in the conduction band could be consumed through a multi-electron reaction with oxygen and finally produce $^\bullet OH$ (E^θ (O_2/H_2O_2) = 0.68 eV vs. NHE, $O_2 + 2H^+ + 2e^- \rightarrow H_2O_2$; $H_2O_2 + e^- \rightarrow OH^- + {}^\bullet OH$), which could accelerate the organic dyes degradation [53,66,67]. Obviously, the directional migration of photogenerated electrons and holes in the 1W/1Ag could prevent the recombination of charge carries in own bulk phase, leading to the improvement of photocatalytic activity due to the location potential change of electrons/holes.

With the exception of photocatalytic activity, it is another important issue to evaluate the stability of photocatalyst from the view of practical application. In order to evaluate the improvement of reusability, the 1W/1Ag and pure Ag_3PO_4 were used to repeatedly degrade the MB and MO solution for three times, respectively. The catalysts should be washed and heated at 80 °C after every cycle until completely dried. The previous investigations showed that pure Ag_3PO_4 would be photochemically decomposed if no sacrificial reagent was involved in photocatalysis. As shown in Fig. 12, the decolourization ratio for MB and MO over pure Ag_3PO_4 greatly decreased after three successive cycling runs and the values reduce to 42% and 53%.

The decline of catalytic activity may be mainly ascribed to two factors. One is the formation of Ag layer on the surface of Ag_3PO_4 due to inevitably reduction of partial Ag^+. The Ag layer can shield light absorption, inhibit the transfer of holes from the valance band of Ag_3PO_4 to the photocatalyst interface, and hinder the contact of Ag_3PO_4 with pollutant molecules [36,53]. The other one is that some secondary inactive substances deposit on the surface of Ag_3PO_4 and blocks the active sites during the photocatalytic degradation process. However, no obvious decrease in photocatalytic activity was observed after three runs during MB and MO photocatalytic degradation, demonstrating the 1W/1Ag composite has excellent recyclability under visible light irradiation. After the third run, the removal rate of MB and MO are still as high as 93% and 87% over 1W/1Ag at the same degradation time. These results obviously investigate that the stability of 1W/1Ag is obviously enhanced compared with pure Ag_3PO_4 catalyst.

4. Conclusions

In this work, a novel 1W/1Ag composite was successfully synthesized using hydrothermal method with two steps and employed in degrading two kinds of organic dye contaminant under visible light. Compared with pure Ag_3PO_4 and WO_3, 1W/1Ag exhibited notably enhanced photocatalytic efficiency. The degradation of MB

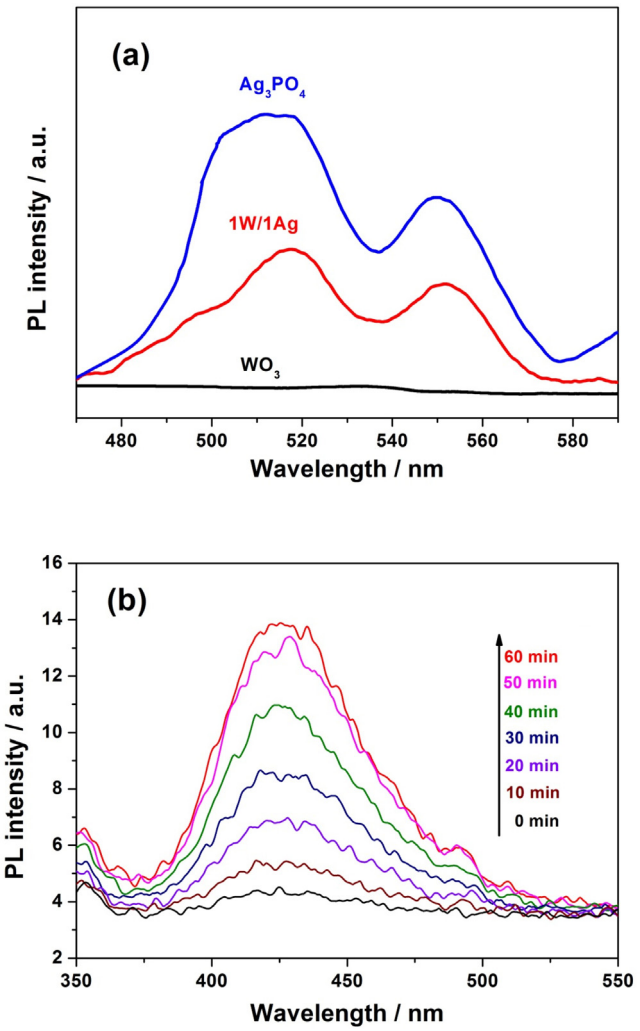

Fig. 11. (a) PL spectral changes observed during illumination for the 1W/1Ag sample in 2×10^{-3} M NaOH solution in the presence of 5×10^{-4} M terephthalic acid, (b) PL spectra of the Ag_3PO_4, 1W/1Ag, and WO_3.

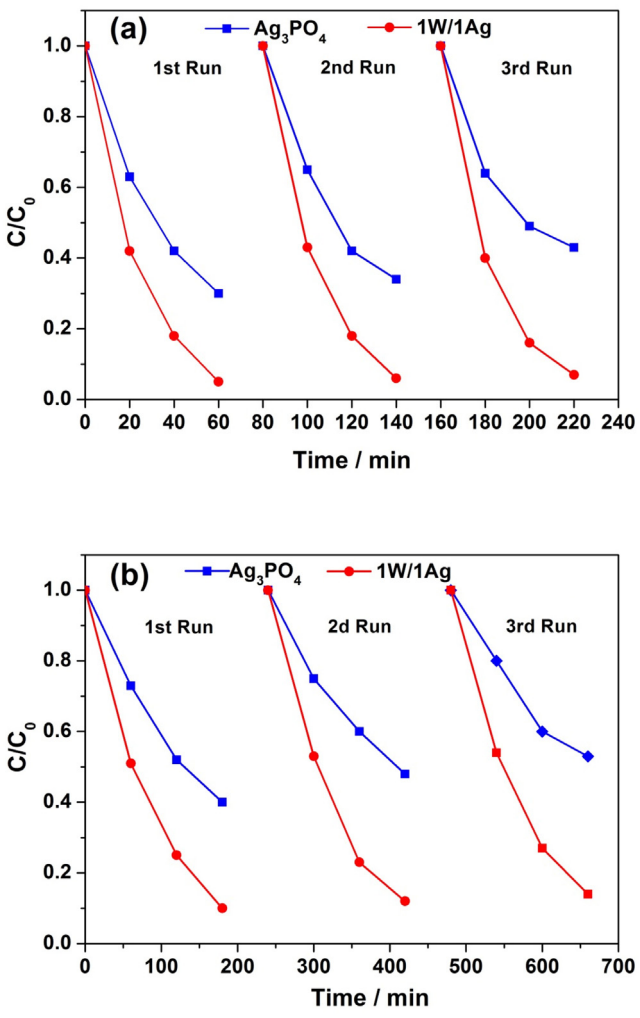

Fig. 12. Photostability and reusability of pure Ag_3PO_4 and 1W/1Ag for degradation of MB (a) and MO (b) under visible light irradiation.

and MO obeyed the pseudo-first-order kinetics. The enhanced photocatalytic performance and stability were attributed to the direct Z-scheme heterojunction structure and synergic effect of Ag_3PO_4 and WO_3, which could be benefit to efficient electron–hole separation and enhanced light energy conversion efficiency. Under visible light illumination, the photoexcited electrons in the conduction band of WO_3 and retained holes in the valence band of Ag_3PO_4 are quickly combined. Meanwhile, the photogenerated holes in the valence band of WO_3 played a major role in oxidation reactions. Undoubtedly, the developing of 1W/1Ag not only improves the reaction activity, but also effectively reduces the cost of the Ag_3PO_4 based photocatalyst, which would be a desired alternative as a simple, efficient, and promising photocatalyst material for wastewater remediation.

Acknowledgments

This work was supported jointly by the National Natural Science Foundation of China (Grant Nos. 21507103, 51508435), the Scientific Research Program Funded by Shaanxi Provincial Education Department (No. 15JK1383), and the Youth Science and Technology Foundation of Xi'an University of Architecture & Technology (No. QN1405).

References

[1] C.M. Teh, A.R. Mohamed, Roles of titanium dioxide and ion-doped titanium dioxide on photocatalytic degradation of organic pollutants (phenolic compounds and dyes) in aqueous solutions: a review, J. Alloys Compd. 509 (2011) 1648–1660.
[2] S.Y. Zhu, S.J. Liang, Y. Wang, X.Y. Zhang, F.Y. Li, H.X. Lin, Z.Z. Zhang, X.X. Wang, Ultrathin nanosheets of molecular sieve SAPO-5: a new photocatalyst for efficient photocatalytic reduction of CO_2 with H_2O to methane, Appl. Catal. B 187 (2016) 11–18.
[3] Y. Chen, S. Zhao, X. Wang, Q. Peng, R. Lin, Y. Wang, R. Shen, X. Cao, L. Zhang, G. Zhou, J. Li, A. Xia, Y. Li, Synergetic integration of $Cu_{1.94}S$–$Zn_xCd_{1-x}S$ heteronanorods for enhanced visible-light-driven photocatalytic hydrogen production, J. Am. Chem. Soc. 138 (2016) 4286–4289.
[4] M.D. Regulacio, M.-Y. Han, Multinary I-III-VI_2 and I_2-II-IV-VI_4 semiconductor nanostructures for photocatalytic applications, Acc. Chem. Res. 49 (2016) 511–519.
[5] E. Grabowska, Selected perovskite oxides: characterization, preparation and photocatalytic properties-a review, Appl. Catal. B 186 (2016) 97–126.
[6] A. Tanaka, K. Hashimoto, H. Kominami, Visible-light-induced hydrogen and oxygen formation over Pt/Au/WO_3 photocatalyst utilizing two types of photoabsorption due to surface plasmon resonance and band-gap excitation, J. Am. Chem. Soc. 136 (2014) 586–589.
[7] M. Zhukovskyi, P. Tongying, H. Yashan, Y. Wang, M. Kuno, Efficient photocatalytic hydrogen generation from Ni nanoparticle decorated CdS nanosheets, ACS Catal. 5 (2015) 6615–6623.
[8] C. Ye, J.-X. Li, Z.-J. Li, X.-B. Li, X.-B. Fan, L.-P. Zhang, B. Chen, C.-H. Tung, L.-Z. Wu, Enhanced driving force and charge separation efficiency of protonated g-C_3N_4 for photocatalytic O_2 evolution, ACS Catal. 5 (2015) 6973–6979.
[9] X. Zong, H. Yan, G. Wu, G. Ma, F. Wen, L. Wang, C. Li, Enhancement of photocatalytic H_2 evolution on CdS by loading MoS_2 as cocatalyst under visible light irradiation, J. Am. Chem. Soc. 130 (2008) 7176–7177.

[10] Q. Xiang, J. Yu, M. Jaroniec, Synergetic effect of MoS_2 and graphene as cocatalysts forenhanced photocatalytic H_2 Production Activity of TiO_2 nanoparticles, J. Am. Chem. Soc. 134 (2012) 6575–6578.
[11] P.P. Jing, J.N. Li, L.N. Pan, J.B. Wang, X.J. Sun, Q.F. Liu, Efficient photocatalytic degradation of acid fuchsin in aqueous solution using separate porous tetragonal-$CuFe_2O_4$ nanotubes, J. Hazard. Mater. 284 (2015) 163–170.
[12] Y. Chen, G. Tian, Z. Ren, K. Pan, Y. Shi, J. Wang, H. Fu, Hierarchical core–shell carbon nanofiber@$ZnIn_2S_4$ composites for enhanced hydrogen evolution performance, ACS Appl. Mater. Interfaces 6 (2014) 13841–13849.
[13] A. Dash, S. Sarkar, V.N.K.B. Adusumalli, V. Mahalingam, Microwave synthesis, photoluminescence, and photocatalytic activity of PVA-functionalized Eu^{3+}-doped BiOX (X = Cl, Br, I) nanoflakes, Langmuir 30 (2014) 1401–1409.
[14] F. Teng, Z. Liu, A. Zhang, M. Li, Photocatalytic performances of Ag_3PO_4 polypods for degradation of dye pollutant under natural indoor weak light irradiation, Environ. Sci. Technol. 49 (2015) 9489–9494.
[15] Y. Bi, S. Ouyang, N. Umezawa, J. Cao, J. Ye, Facet effect of single-crystalline Ag_3PO_4 sub-microcrystals on photocatalytic properties, J. Am. Chem. Soc. 133 (2011) 6490–6492.
[16] X.J. Chen, Y.Z. Dai, X.Y. Wang, Methods and mechanism for improvement of photocatalytic activity and stability of Ag_3PO_4: a review, J. Alloys Compd. 649 (2015) 910–932.
[17] Q. Wu, P.F. Wang, F.T. Niu, C.P. Huang, Y. Li, W.F. Yao, A novel molecular sieve supporting material for enhancing activity and stability of Ag_3PO_4 photocatalyst, Appl. Surf. Sci. 378 (2016) 552–563.
[18] Z. Yi, J. Ye, N. Kikugawa, T. Kako, S. Ouyang, H. Stuart-Williams, H. Yang, J. Cao, W. Luo, Z. Li, Y. Liu, R.L. Withers, An orthophosphate semiconductor with photooxidation properties under visible-light irradiation, Nat. Mater. 9 (2010) 559–564.
[19] J.J. Liu, X.L. Fu, S.F. Chen, Y.F. Zhu, Electronic structure and optical properties of Ag_3PO_4 photocatalyst calculated by hybrid density functional method, Appl. Phys. Lett. 99 (2011).
[20] B.J. Zheng, X. Wang, C. Liu, K. Tan, Z.X. Xie, L.S. Zheng, High-efficiently visible light-responsive photocatalysts: Ag_3PO_4 tetrahedral microcrystals with exposed {111} facets of high surface energy, J. Mater. Chem. A 1 (2013) 12635–12640.
[21] Z.B. Jiao, Y. Zhang, H.C. Yu, G.X. Lu, J.H. Ye, Y.P. Bi, Concave trisoctahedral Ag_3PO_4 microcrystals with high-index facets and enhanced photocatalytic properties, Chem. Commun. 49 (2013) 636–638.
[22] Y.P. Bi, H.Y. Hu, S.X. Ouyang, G.X. Lu, J.Y. Cao, J.H. Ye, Photocatalytic and photoelectric properties of cubic Ag_3PO_4 sub-microcrystals with sharp corners and edges, Chem. Commun. 48 (2012) 3748–3750.
[23] Y. Xie, Z. Huang, Z. Zhang, X. Zhang, R. Wen, Y. Liu, M. Fang, X. Wu, Controlled synthesis and photocatalytic properties of rhombic dodecahedral Ag_3PO_4 with high surface energy, Appl. Surf. Sci. 389 (2016) 56–66.
[24] X.Y. Li, R.J. Zheng, Q.Z. Luo, D.S. Wang, J. An, R. Yin, Y.Y. Liu, D. Wu, X.M. Han, Cyclized polyacrynitrile modified Ag_3PO_4 photocatalysts with enhanced photocatalytic activity under visible-light irradiation, Appl. Surf. Sci. 356 (2015) 941–950.
[25] W.J. Fa, P. Wang, B. Yue, F.L. Yang, D.P. Li, Z. Zheng, Ag_3PO_4/Ag_2CO_3 p-n heterojunction composites with enhanced photocatalytic activity under visible light, Chin. J. Catal. 36 (2015) 2186–2193.
[26] K. Maeda, Z-scheme Water Splitting using two different semiconductor photocatalysts, ACS Catal. 3 (2013) 1486–1503.
[27] D.M. Fabian, S. Hu, N. Singh, F.A. Houle, T. Hisatomi, K. Domen, F.E. Osterlohf, S. Ardo, Particle suspension reactors and materials for solar-driven water splitting, Energy Environ. Sci. 8 (2015) 2825–2850.
[28] S. Bai, J. Jiang, Q. Zhang, Y.J. Xiong, Steering charge kinetics in photocatalysis: intersection of materials syntheses, characterization techniques and theoretical simulations, Chem. Soc. Rev. 44 (2015) 2893–2939.
[29] Y. Sasaki, A. Iwase, H. Kato, A. Kudo, The effect of co-catalyst for Z-scheme photocatalysis systems with an Fe^{3+}/Fe^{2+} electron mediator on overall water splitting under visible light irradiation, J. Catal. 259 (2008) 133–137.
[30] M. Tabata, K. Maeda, M. Higashi, D.L. Lu, T. Takata, R. Abe, K. Domen, Modified Ta_3N_5 powder as a photocatalyst for O^{-2} evolution in a two-step water splitting system with an Iodate/Iodide shuttle redox mediator under visible light, Langmuir 26 (2010) 9161–9165.
[31] Y. Sasaki, H. Kato, A. Kudo, $Co(bpy)^{33+/2+}$ and $Co(phen)^{33+/2+}$ electron mediators for overall water splitting under sunlight irradiation using Z-scheme photocatalyst system, J. Am. Chem. Soc. 135 (2013) 5441–5449.
[32] H. Tada, T. Mitsui, T. Kiyonaga, T. Akita, K. Tanaka, All-solid-state Z-scheme in CdS-Au-TiO_2 three-component nanojunction system, Nat. Mater. 5 (2006) 782–786.
[33] A. Iwase, Y.H. Ng, Y. Ishiguro, A. Kudo, R. Amal, Reduced graphene oxide as a solid-state electron mediator in Z-scheme photocatalytic water splitting under visible light, J. Am. Chem. Soc. 133 (2011) 11054–11057.
[34] A. Samal, D.P. Das, K.K. Nanda, B.K. Mishra, J. Das, A. Dash, Reduced graphene oxide-Ag_3PO_4 heterostructure: a direct Z-scheme photocatalyst for augmented photoreactivity and stability, Chem.—Asian J. 11 (2016) 584–595.
[35] S.G. Meng, X.F. Ning, T. Zhang, S.F. Chen, X.L. Fu, What is the transfer mechanism of photogenerated carriers for the nanocomposite photocatalyst Ag_3PO_4/g-C3N4, band-band transfer or a direct Z-scheme? Phys. Chem. Chem. Phys. 17 (2015) 11577–11585.
[36] X.X. Chen, X.T. Huang, Z.G. Yi, Enhanced ethylene photodegradation performance of g-C_3N_4-Ag_3PO_4 composites with direct Z-scheme configuration, Chem.—Eur. J. 20 (2014) 17590–17596.
[37] O. Arutanti, A.B.D. Nandiyanto, T. Ogi, T.O. Kim, K. Okuyama, Influences of porous structurization and Pt addition on the improvement of photocatalytic performance of WO_3 particles, ACS Appl. Mater. Interfaces 7 (2015) 3009–3017.
[38] F. Amano, E. Ishinaga, A. Yamakata, Effect of particle size on the photocatalytic activity of WO_3 particles for water oxidation, J. Phys. Chem. C 117 (2013) 22584–22590.
[39] L. Wang, Y. Chai, J. Ren, J. Ding, Q. Liu, W.-L. Dai, Ag_3PO_4 nanoparticles loaded on 3D flower-like spherical MoS_2: a highly efficient hierarchical heterojunction photocatalyst, Dalton Trans. 44 (2015) 14625–14634.
[40] N.K. Eswar, V.V. Katkar, P.C. Ramamurthy, G. Madras, Novel AgBr/Ag_3PO_4 decorated ceria nanoflake composites for enhanced photocatalytic activity toward dyes and bacteria under visible light, Ind. Eng. Chem. Res. 54 (2015) 8031–8042.
[41] J. Ding, Y.Y. Chai, Q.Q. Liu, X. Liu, J. Ren, W.L. Dai, Selective deposition of silver nanoparticles onto WO_3 nanorods with different facets: the correlation of facet-induced electron transport preference and photocatalytic activity, J. Phys. Chem. C 120 (2016) 4345–4353.
[42] W.G. Wang, B. Cheng, J.G. Yu, G. Liu, W.H. Fan, Visible-light photocatalytic activity and deactivation mechanism of Ag_3PO_4 spherical particles, Chem.—Asian J. 7 (2012) 1902–1908.
[43] J. Zhang, Y. Hu, X. Jiang, S. Chen, S. Meng, X. Fu, Design of a direct Z-scheme photocatalyst: preparation and characterization of Bi_2O_3/g-C_3N_4 with high visible light activity, J. Hazard. Mater. 280 (2014) 713–722.
[44] C. Wang, M. Wu, M. Yan, H. Shen, F. Cai, B. Hua, W. Shi, Enhanced visible-light photocatalytic activity and the mechanism study of WO_3 nanosheets coupled with Ag_3PO_4 nanocrystals, Ceram. Int. 41 (2015) 6784–6792.
[45] S. Emin, M. de Respinis, M. Fanetti, W. Smith, M. Valant, B. Dam, A simple route for preparation of textured WO_3 thin films from colloidal W nanoparticles and their photoelectrochemical water splitting properties, Appl. Catal. B 166 (2015) 406–412.
[46] K.S. Ahn, S.H. Lee, A.C. Dillon, C.E. Tracy, R. Pitts, The effect of thermal annealing on photoelectrochemical responses of WO_3 thin films, J. Appl. Phys. 101 (2007).
[47] C.S. Zhu, L. Zhang, B. Jiang, J.T. Zheng, P. Hu, S.J. Li, M.B. Wu, W.T. Wu, Fabrication of Z-scheme Ag_3PO_4/MoS_2 composites with enhanced photocatalytic activity and stability for organic pollutant degradation, Appl. Surf. Sci. 377 (2016) 99–108.
[48] Z. Chen, W. Wang, Z. Zhang, X. Fang, High-efficiency visible-light-driven Ag_3PO_4/AgI photocatalysts: Z-scheme photocatalytic mechanism for their enhanced photocatalytic activity, J. Phys. Chem. C 117 (2013) 19346–19352.
[49] J. Ding, Q.Q. Liu, Z.Y. Zhang, X. Liu, J.Q. Zhao, S.B. Cheng, B.N. Zong, W.L. Dai, Carbon nitride nanosheets decorated with WO_3 nanorods: ultrasonic-assisted facile synthesis and catalytic application in the green manufacture of dialdehydes, Appl. Catal. B 165 (2015) 511–518.
[50] X.X. Zou, G.D. Li, P.P. Wang, J. Su, J. Zhao, L.J. Zhou, Y.N. Wang, J.S. Chen, A precursor route to single-crystalline WO_3 nanoplates with an uneven surface and enhanced sensing properties, Dalton Trans. 41 (2012) 9773–9780.
[51] J. Cao, B.D. Luo, H.L. Lin, B.Y. Xu, S.F. Chen, Thermodecomposition synthesis of WO_3/H_2WO_4 heterostructures with enhanced visible light photocatalytic properties, Appl. Catal. B 111 (2012) 288–296.
[52] B. Chai, J. Li, Q. Xu, Reduced graphene oxide grafted Ag_3PO_4 Composites with efficient photocatalytic activity under visible-light irradiation, Ind. Eng. Chem. Res. 53 (2014) 8744–8752.
[53] J.Q. Zhang, K. Yu, Y.F. Yu, L.L. Lou, Z.Q. Yang, J.W. Yang, S.X. Liu, Highly effective and stable Ag_3PO_4/WO_3 photocatalysts for visible light degradation of organic dyes, J. Mol. Catal. A: Chem. 391 (2014) 12–18.
[54] Y. Chang, K. Yu, C.X. Zhang, R. Li, P.Y. Zhao, L.L. Lou, S.X. Liu, Three-dimensionally ordered macroporous WO_3 supported Ag_3PO_4 with enhanced photocatalytic activity and durability, Appl. Catal. B 176 (2015) 363–373.
[55] K. Mahmood, B.S. Swain, A.R. Kirmani, A. Amassian, Highly efficient perovskite solar cells based on a nanostructured WO_3.TiO_2 core-shell electron transporting material, J. Mater. Chem. A 3 (2015) 9051–9057.
[56] J. Jin, J.G. Yu, D.P. Guo, C. Cui, W.K. Ho, A hierarchical Z-scheme CdS-WO_3 photocatalyst with enhanced CO_2 reduction activity, Small 11 (2015) 5262–5271.
[57] J. Lv, K. Dai, J.F. Zhang, L. Geng, C.H. Liang, Q.C. Liu, G.P. Zhu, C. Chen, Facile synthesis of Z-scheme graphitic-C_3N_4/Bi_2MoO_6 nanocomposite for enhanced visible photocatalytic properties, Appl. Surf. Sci. 358 (2015) 377–384.
[58] J.G. Yu, S.H. Wang, J.X. Low, W. Xiao, Enhanced photocatalytic performance of direct Z-scheme g-C_3N_4-TiO_2 photocatalysts for the decomposition of formaldehyde in air, Phys. Chem. Chem. Phys. 15 (2013) 16883–16890.
[59] W.L. Yu, D.F. Xu, T.Y. Peng, Enhanced photocatalytic activity of g-C_3N_4 for selective CO_2 reduction to CH_3OH via facile coupling of ZnO: a direct Z-scheme mechanism, J. Mater. Chem. A 3 (2015) 19936–19947.
[60] W.J. Li, D.Z. Li, Y.M. Lin, P.X. Wang, W. Chen, X.Z. Fu, Y. Shao, Evidence for the active species involved in the photodegradation process of methyl orange on TiO_2, J. Phys. Chem. C 116 (2012) 3552–3560.
[61] Y.M. Lin, D.Z. Li, J.H. Hu, G.C. Xiao, J.X. Wang, W.J. Li, X.Z. Fu, Highly efficient photocatalytic degradation of organic pollutants by PANI-modified TiO_2 composite, J. Phys. Chem. C 116 (2012) 5764–5772.

[62] S.G. Kumar, K. Rao, Tungsten-based nanomaterials (WO_3 & Bi_2WO_6): modifications related to charge carrier transfer mechanisms and photocatalytic applications, Appl. Surf. Sci. 355 (2015) 939–958.
[63] P. Zhou, J.G. Yu, M. Jaroniec, All-solid-state Z-scheme photocatalytic systems, Adv. Mater. 26 (2014) 4920–4935.
[64] Y.N. Liu, R.X. Wang, Z.K. Yang, H. Du, Y.F. Jiang, C.C. Shen, L.A. Kuang, A.W. Xu, Enhanced visible-light photocatalytic activity of Z-scheme graphitic carbon nitride/oxygen vacancy-rich zinc oxide hybrid photocatalysts, Chin. J. Catal. 36 (2015) 2135–2144.
[65] W. Chen, T.Y. Liu, T. Huang, X.H. Liu, J.W. Zhu, G.R. Duan, X.J. Yang, In situ fabrication of novel Z-scheme Bi_2WO_6 quantum dots/g-C3N4 ultrathin nanosheets heterostructures with improved photocatalytic activity, Appl. Surf. Sci. 355 (2015) 379–387.
[66] J. Kim, C.W. Lee, W. Choi, Platinized WO_3 as an environmental photocatalyst that generates OH radicals under visible light, Environ. Sci. Technol. 44 (2010) 6849–6854.
[67] S.B. Rawal, S.D. Sung, W.I. Lee, Novel Ag_3PO_4/TiO_2 composites for efficient decomposition of gaseous 2-propanol under visible-light irradiation, Catal. Commun. 17 (2012) 131–135.